

Active VLF transmission experiments between the DSX and VPM spacecraft

Riley A. Reid¹, Robert A. Marshall¹, Michael J. Starks², Maria E. Usanova³,
Gordon R. Wilson², W. Robert Johnston², Jenny C. Sanchez², Yi-Jiun Su²,
Gregory P. Ginet⁴, Paul Song⁵, Ivan A. Galkin⁵

¹Department of Aerospace Engineering Sciences, University of Colorado, Boulder, Colorado, United States

²Air Force Research Laboratory, Space Vehicles Directorate, Kirtland Air Force Base, New Mexico,
United States

³Laboratory for Atmospheric and Space Physics, University of Colorado, Boulder, Colorado, United
States

⁴MIT Lincoln Laboratory, Lexington, Massachusetts, United States

⁵University of Massachusetts, Lowell, Massachusetts, United States

Key Points:

- Results from active conjunction experiments between DSX and VPM are presented
- Ray-tracing is performed to investigate the lack of DSX signal observation
- The effects of the antenna efficiency and plasmasphere model are explored

Abstract

This study presents results from magnetic field line conjunctions between the medium-Earth orbiting Demonstration and Science Experiments (DSX) satellite and the low-Earth orbiting VLF Propagation Mapper (VPM) satellite. DSX transmitted at very low frequencies (VLF) towards VPM, which was equipped with a single-axis dipole electric field antenna, when the two spacecraft passed near the same magnetic field line. VPM did not observe DSX signals in any of the 27 attempted conjunction experiments; the goal of this study, therefore, is to explain why DSX signals were not received. Explanations include i) the predicted power at LEO from DSX transmissions was too low for VPM to observe; ii) VPM's trajectory missed the "spot" of highest intensity due to the focused ray paths reaching LEO; or iii) rays mirrored before reaching VPM. Different combinations of these explanations are found. We present ray-tracing analysis for each conjunction event to predict the distribution of power and wave normal angles in the vicinity of VPM at LEO altitudes. We find that, for low-frequency (below 4 kHz) transmissions, nearly all rays mirror before reaching LEO, resulting in low amplitudes at LEO. For mid- and high-frequency transmissions (~ 8 kHz and 28 kHz respectively), the power at LEO is above the noise threshold of the VPM receiver (between $0.5 \mu\text{V/m}$ and $1 \mu\text{V/m}$). We conclude that the antenna efficiency and plasmasphere model are critical in determining the predicted power at LEO, and are also the two most significant sources of uncertainty that could explain the apparent discrepancy between predicted amplitudes and VPM observations.

Plain Language Summary

In this study we present results from transmissions between two near-Earth spacecraft. The Demonstration and Science Experiments (DSX) satellite transmitted signals at very low radio frequencies (VLF) towards the VLF Propagation Mapper (VPM) satellite when the two satellites passed near the same magnetic field line. VLF broadcasts tend to follow magnetic field lines as they are guided by the plasma in the magnetosphere. This study is important for understanding VLF wave propagation in the near-Earth space environment. We analyze the data from each experiment and conclude that DSX broadcasts were not observed by VPM. The goal of this paper is to describe our analysis to explain possible reasons for the lack of observation. We perform ray-tracing, or solving for the paths of the VLF broadcasts, to explain why VPM missed the signals. We conclude that in some cases, the broadcasts mirrored, or reversed direction in the near-Earth space environment before they were able to reach VPM. In other cases, the ray-tracing analysis predicts we should have observed the signals. However, we find that the DSX antenna performance and the model of the near-Earth environment we use in these simulations are significant sources of uncertainty that could explain this discrepancy.

1 Introduction

Very low frequency (3–30 kHz, VLF) waves can significantly impact the evolution of energetic particle distributions in near-Earth space. VLF waves originate from ground-based sources, such as lightning and VLF transmitters, and waves generated in the magnetosphere such as chorus and hiss. These waves propagate through the magnetosphere as whistler-mode waves, which can induce precipitation of trapped energetic particles, impacting atmospheric chemistry, astronaut safety, and satellite operations (Verronen et al., 2013; Horne et al., 2013). To better understand the impact of VLF energy on energetic particle populations, we study the propagation of whistler-mode waves in the magnetosphere. VLF wave propagation characteristics such as wave direction, amplitude, and wave normal angle can influence whether or not a VLF wave is likely to induce particle precipitation (Kulkarni et al., 2007, 2008; Rodger et al., 2010).

68 Observing VLF wave propagation requires multi-point measurements to deduce the
 69 source and resulting path. These studies often impose precise timing and navigation re-
 70 quirements on spacecraft. A recent study by Colpitts et al. (2020) was the first direct
 71 observation of the propagation of chorus elements from the equatorial source region to
 72 a higher magnetic latitude through simultaneous observations from the Van Allen Probes
 73 and Arase spacecraft. This study was possible because of the close magnetic conjunc-
 74 tion that allowed the two satellites to be in the right places at the right time; the actual
 75 chorus element observation lasted less than a minute.

76 Compared to naturally occurring VLF emissions, ground-based VLF transmitters
 77 present a unique opportunity to study VLF propagation. Ground-based VLF transmit-
 78 ters, operated by the US Navy and other Navies, are located worldwide and transmit con-
 79 tinuously at known discrete frequency bands, allowing their respective signals to be eas-
 80 ily identifiable in satellite-based observations. Numerous previous studies have presented
 81 observations of active ground-based VLF transmitters from satellites in the magneto-
 82 sphere (Sauvaud et al., 2008; Zhang et al., 2018; Ma et al., 2017; Cohen & Inan, 2012).
 83 These studies are often supported by ray-tracing analysis to reproduce possible paths
 84 of the VLF signals and reveal propagation characteristics. However, ground-based VLF
 85 transmitters only exist at specific locations, and most transmit at frequencies above 15 kHz,
 86 with the majority transmitting between 18 kHz and 26 kHz. Frequency and source lo-
 87 cation are significant drivers in the propagation path, thereby affecting the particle pop-
 88 ulations that the wave might influence (Starks et al., 2009, 2020). Satellite-based trans-
 89 missions, however, allow for the control of source location, frequency, and amplitude, as
 90 well as the opportunity to better understand the propagation of natural inner-magnetosphere
 91 sourced VLF waves, such as hiss and chorus.

92 We build on these previous studies of VLF propagation from natural sources and
 93 from ground-based VLF transmitters by presenting active experiments from a satellite-
 94 based VLF transmitter. We present results from active VLF transmission experiments
 95 between the medium-Earth orbiting Demonstration and Science Experiments (DSX) space-
 96 craft and the low-Earth orbit Very Low Frequency Propagation Mapper (VPM) Cube-
 97 Sat. The following section briefly describes the missions, while Section 2 describes the
 98 data collected during 27 conjunction experiments. Section 2 also details data analysis
 99 performed, leading to the conclusion that no DSX signals were observed in any of the
 100 27 events. The remainder of this paper presents ray-tracing analysis to simulate each con-
 101 junction and investigate the lack of DSX signal observation. Section 3 describes the meth-
 102 ods used to perform these simulations, while Sections 4 and 5 describe the results for each
 103 case.

104 1.1 The DSX and VPM Missions

105 The Air Force Research Laboratory (AFRL)’s Demonstration and Science Exper-
 106 iments (DSX) mission launched in 2019 to research the medium-Earth Orbit (MEO) ra-
 107 diation environment for improved operation of satellites (Scherbarth et al., 2009). DSX
 108 was launched into an elliptical orbit with a perigee of 6000 km and an apogee of 12000 km
 109 and a 42° inclination. Onboard DSX is the Wave Particle Interactions Experiment (WPIx),
 110 intended to study VLF transmissions in the magnetosphere and their impact on ener-
 111 getic particle populations. DSX performed conjunction experiments with several other
 112 missions in addition to VPM to support this science goal, including the Japan Aerospace
 113 Exploration Agency Arase satellite, for which data analysis is ongoing. A component of
 114 the WPIx experiment is an 80 meter dipole antenna that can broadcast in the 1–50 kHz
 115 range while drawing at most 1 kW of power (Spanjers et al., 2006).

116 The Very Low Frequency Propagation Mapper (VPM) mission is a companion satel-
 117 lite in low-Earth orbit (LEO) supporting the WPIx scientific objective by attempting
 118 to measure transmissions from the WPIx dipole antenna and characterize the transmit-

ting antenna radiation pattern (Marshall et al., 2021). VPM is a 6U CubeSat carrying a single-axis electric field dipole, with an effective length of 1.1 meters, and a single-axis magnetic field search coil antenna. VPM was deployed into a 500 km orbit with 51.6° inclination in February 2020, and the electric field antennas deployed on March 6, 2020. On March 10, 2020, the search coil deployment was first attempted. Burst mode data collected during the attempted deployment indicated no change in data quality, with the data continuing to suffer from spacecraft noise that obscures any natural signals, as expected for an undeployed antenna. Despite further deployment attempts in the coming months, the signal quality did not change, indicating a likely failure of deployment. Therefore, only the electric field data is used for this study.

From April 2020 to August 2020, several magnetic field line conjunctions occurred in which DSX passed near the same magnetic field line as VPM in their respective orbits. Conjunctions were predicted using the IGRF-13 magnetic field model (Alken et al., 2021). Of these conjunctions, real-time currents and voltages from the DSX antenna exists for 27 events confirming that the DSX antenna successfully transmitted. Contact was lost with VPM in September 2020, and therefore no further conjunction experiments were attempted.

2 VPM Data Analysis

VPM collected burst mode data with an 80 kHz sampling rate during each magnetic conjunction. The bursts lasted approximately 100 seconds as VPM made its closest pass to the estimated DSX magnetic field line footpoint. Bursts have a windowing pattern in which data is collected for 10 seconds and then data collection pauses for 2, 5, or 10 seconds before the pattern repeats, with up to a total of 60 seconds of data collected (Marshall et al., 2021).

Confirmed transmission data for each conjunction also indicates the frequency pattern transmitted. These specific frequency patterns can be used to identify signatures of DSX in the VPM burst data. However, signals leaving DSX will undergo a Doppler shift from the motion of both DSX and VPM relative to the expected wave-vector of the transmitted or received wave. This shift can be significant; the recent study by Némec et al. (2021) observed Doppler shifts as significant as two percent from observations of VLF transmitters by the LEO spacecraft DEMETER. During DSX-VPM magnetic conjunctions, the signals will incur a Doppler shift when leaving DSX and an additional Doppler shift arriving at LEO due to the change in the index of refraction and the velocity of the satellites.

We calculate expected Doppler shifts of signals using ray-tracing analysis. DSX transmitted in three frequency regimes throughout this experiment: low (2–4 kHz), medium (~ 8 kHz), and high (28 kHz). We propagate ray paths to track the change in the index of refraction vector and calculate the expected total Doppler shift due to the satellite’s velocity during magnetic conjunctions. In the analyzed cases, the expected Doppler shift was found to be no more than 100 Hz for an 8.2 kHz signal or about 1.5 %. Therefore, we expect Doppler shifts during these conjunctions within 50 Hz in the low-frequency regime, within 100 Hz in the medium regime, and within 400 Hz in the high regime.

Signals will also experience a significant time delay due to the propagation time from DSX to VPM. Throughout the 27 experiments, the magnetic field line separation varied between 6,400 km and 27,000 km. By also computing the expected group velocity through ray-tracing, we anticipate the expected propagation time from DSX to VPM and find it to be a few hundred milliseconds at most. With the range of theoretical Doppler shift, time delay, and transmission patterns leaving DSX for each case, we analyze VPM’s data during each conjunction.

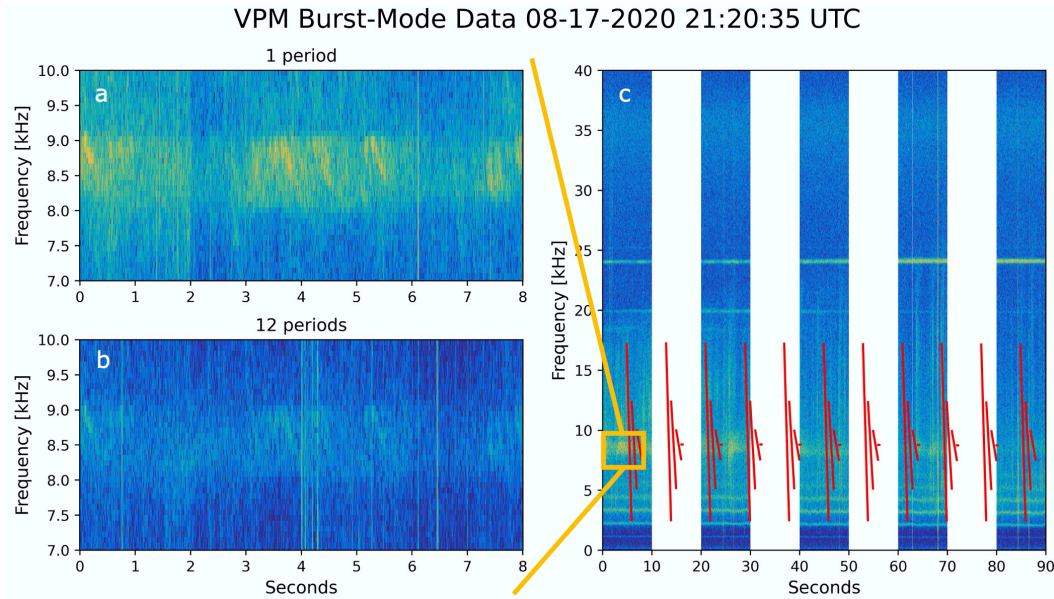


Figure 1. VPM burst mode electric field data from August 17, 2020, at 21:30:35 UT. Panel c shows burst mode data, with the DSX transmission pattern overlaid in red. The insets show results from superposed epoch analysis, with panel a showing the first eight seconds of the burst and panel b showing the result of averaging twelve eight-second periods of burst mode data.

168 First, we estimate the minimum detectable signal amplitude for each burst obser-
 169 vation, which depends on the system sensitivity. This sensitivity changes due to vari-
 170 ations in spacecraft noise; for example, when sunlit the spacecraft experiences increased
 171 solar panel noise. The expected Doppler shift for each frequency regime allows us to ap-
 172 propriately size the frequency bin width when processing each burst. When processing
 173 the burst-mode data, we add an artificial signal at the transmission frequency. This sig-
 174 nal undergoes amplitude spreading by adjusting the Fast Fourier transform length to match
 175 the predicted bin width from the theoretical Doppler shift. By decreasing the amplitude
 176 of the artificial signal until the signal is lost to the noise floor, we can estimate the min-
 177 imum detectable signal. These results are shown in the rightmost column of Table 1, and
 178 inform our expectations of the DSX signal. These results are discussed further in the re-
 179 mainder of the paper.

180 We found only one case with signals resembling DSX’s transmission pattern dur-
 181 ing a magnetic field line conjunction; this case occurred on August 17, 2020. VPM burst-
 182 mode data for this event is shown in Figure 1c, with the DSX transmission pattern over-
 183 laid as red lines. During this particular conjunction, DSX transmitted in a “Resonance
 184 Discovery” pattern, in which large frequency sweeps are performed at the antenna to iden-
 185 tify the resonant frequency. The antenna then radiates short pulses of high intensity at
 186 the resonant frequency, which is 8.8 kHz for this particular conjunction. Due to a tim-
 187 ing uncertainty onboard DSX, the exact timing of these pulses is unknown within a few
 188 seconds. Even with knowledge of the propagation time, we can’t be certain of the align-
 189 ment of these transmissions to the signals observed. Therefore, we identify this specific
 190 case on August 17, 2020 as one of interest because the signals in the VPM data are in
 191 the anticipated frequency region, considering a possible Doppler shift of 100 Hz and ex-
 192 pected delay in time between the pulses.

DSX repeats these resonance patterns every eight seconds. To confirm this signal was from DSX and not a natural emission, we performed superposed epoch analysis on the data. This analysis reveals any periodic signals indicative of a repeating frequency pattern. Figure 1a shows the first eight seconds of the VPM burst mode data, while Figure 1b shows the result of averaging twelve eight-second periods of the burst mode data. Figure 1b shows a lower noise floor and a lower intensity of the signals near 9 kHz. The lower signal intensity indicates the signals did not repeat in eight-second periods, making it unlikely that the signals originated from DSX. Even though DSX may travel upwards of 50 km in eight seconds, it is unlikely that the observed signals are DSX. The observed signals cover a much more extensive frequency range than can be explained by Doppler shifts. The frequency ramp transmissions performed by the DSX antenna are likely too weak to be observed, and the high-power, short-pulse transmissions are expected to have no more than 100 Hz Doppler shift, in contrast to the 500 Hz shift observed.

Therefore, as August 17, 2020 is the only case with visible signals resembling DSX, we conclude that VPM did not observe DSX signals in any of the 27 conjunctions. Further analysis revealed that the signals observed on August 17 might be part of wedge-like structures formed by upper and lower VLF cutoff frequencies that are dependent on the local lower hybrid resonance frequency (Shklyar et al., 2010).

3 Methods

We turn to ray-tracing analysis to investigate the lack of DSX signal observation. We hypothesize that i) the predicted power at LEO from DSX transmissions was too low for VPM to observe, i.e., the signal was below our sensitivity; ii) VPM's trajectory missed the relatively small "spot" of highest intensity due to the focused ray paths reaching LEO; iii) rays mirrored before reaching 500 km altitude, thus never reaching VPM's orbit; or iv) some combination of these three effects. Ray tracing analysis allows us to predict the propagation path DSX transmissions took and track the wave attenuation due to Landau damping. In addition, we chose to ray-trace in two different model plasmaspheres to estimate the uncertainty of the predicted power and spatial ray "spot" from our results, as the models represent a range of possible plasma environments that may have existed during DSX-VPM conjunctions.

3.1 Geophysical Models

Ray paths are modeled in three dimensions using the Stanford VLF Ray Tracing program (Inan & Bell, 1977), which has been used extensively and updated (such as updating from two to three dimensions) in many VLF propagation studies (Bell et al., 2002; Inan et al., 2003; Bortnik et al., 2007; Kulkarni et al., 2008). The Stanford ray tracer computes ray propagation paths in the International Geomagnetic Reference Field (IGRF) 13th Generation magnetic field model in two different plasmasphere models: Diffusive Equilibrium (Angerami & Thomas, 1964) and the Global Core Plasma Model (Gallagher et al., 2000). The Diffusive Equilibrium model is an analytical model that approximates the local plasma density distribution through a diffusive equilibrium distribution. The Global Core Plasma Model is an empirical model that combines separate models for the ionosphere, plasmasphere, plasmopause, trough, and polar cap. The International Reference Ionosphere version 16 is used for the ionosphere model in GCPM (Bilitza, 2001). Because DSX signals were transmitted from MEO from L-shells 2–4, outer plasmasphere features are not relevant to compute the ray paths from DSX to LEO. Therefore, a simplified version of GCPM is implemented that assumes constant electron density along each field line, removes the polar cap model, and merges the ionosphere into the equatorial trough model with empirical fits applied to IRI to smoothly transition between the dayside and nightside (Sousa, 2018).

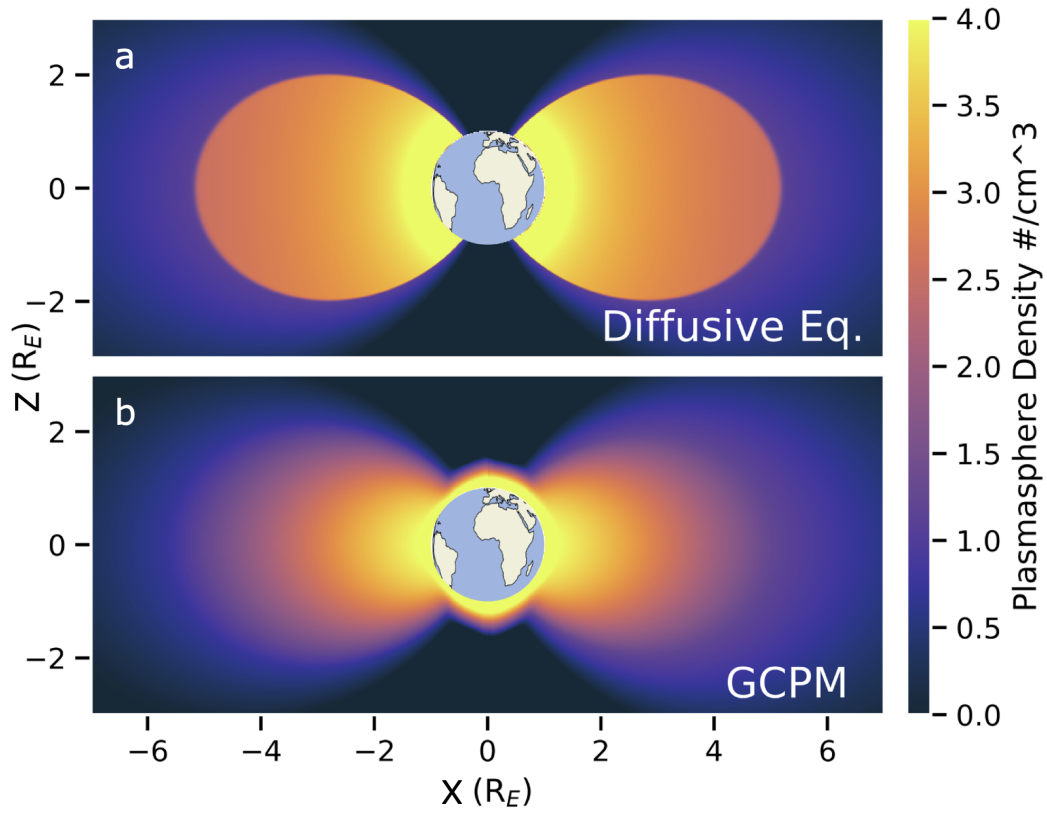


Figure 2. Plasmasphere density in the Diffusive Equilibrium model (panel a) and the Global Core Plasmaphere model (panel b).

Figure 2 shows meridional electron density for the Diffusive Equilibrium model and the simplified GCPM model (referred to as GCPM for the remainder of the paper). Both models use a Carpenter-Anderson based model of plasmopause location (Carpenter & Anderson, 1992) that determines plasmopause location based on the geomagnetic activity index Kp. By extracting hourly Kp values from NASA/GSFC’s OMNI data set through OMNIWeb for each of the 27 events, we found the median Kp value to be 1. Therefore, the simulations in this paper are performed with $Kp = 1$. Consequently, the plasmopause location is not very relevant to our results, as most DSX-VPM conjunctions occurred at low L-shell values during periods of low geomagnetic activity; in other words, most conjunctions occurred well within the plasmopause. The two exceptions to this are discussed in further in Section 4. Figure 2 also clearly shows the difference in density gradients between the models. The Diffusive Equilibrium has a particularly steep density gradient at low altitudes compared to GCPM, the effects of which are discussed further in Section 5.

3.2 Landau Damping

We also compute the attenuation of the rays through Landau damping, which is dependent upon the propagation medium (Brinca, 1972). The implementation of Landau damping in the Stanford ray tracer remains the same as that described in the thesis work of Bortnik (2004). Most DSX-VPM conjunctions occurred where both satellites were in the same magnetic hemisphere; in these cases, Landau damping calculations resulted in very minor attenuation of less than 1%. Landau damping results in more significant attenuation for magnetic conjunctions in the opposite hemisphere in which ray paths cross the magnetic equator.

3.3 Antenna Model

To simulate the DSX antenna radiation efficiency as a function of initial wave normal angle, we start by initializing rays at DSX’s location during the magnetic conjunctions. Each ray is initialized with a random initial direction, corresponding to the initial wave normal angle, the angle between the wave-vector \vec{k} and the local magnetic field \vec{B} . The wave normal angles are constrained to be within the local resonance cone, which depends on the transmission frequency and the local plasma density. Figure 3 visualizes this concept by showing the refractive index surfaces for a ray initialized at DSX with a frequency of 2.8 kHz for the June 6, 2020 DSX-VPM conjunction. In Figure 3c the resonance cone is shown as the blue shaded region and indicates the range of possible propagating wave normal angles. For this ray, the initial wave normal angle is a few degrees from field-aligned, shown by the direction of the wave-vector \vec{k} . The wave-vector is related to the index of refraction as $\vec{k} = \frac{\omega}{c}\vec{n}$ where ω is wave frequency.

The ray is then weighted by the antenna radiation efficiency η . In the absence of a complete analytical or numerical description of the radiation pattern of this antenna, as a first approximation we base this efficiency on the radiation pattern for a small dipole antenna and its dependence on wavelength. This efficiency is inversely proportional to the square of the wavelength, and the wavelength is proportional to the index of refraction, \vec{n} ; hence, near the resonance cone, where the index of refraction becomes very large and the wavelength very short, the antenna radiation efficiency is higher. Therefore, we define the antenna radiation efficiency η as the ratio of the squared magnitudes of the index of refraction of the ray at DSX n_{DSX} and the index of refraction near the resonance cone n_{res} , given by Equation 1:

$$\eta = \left(\frac{n_{DSX}}{n_{res}}\right)^2 \quad (1)$$

The wave normal angle is directly related to the index of refraction as previously discussed, and therefore η is dependent on initial wave normal angle. Physically, this ref-

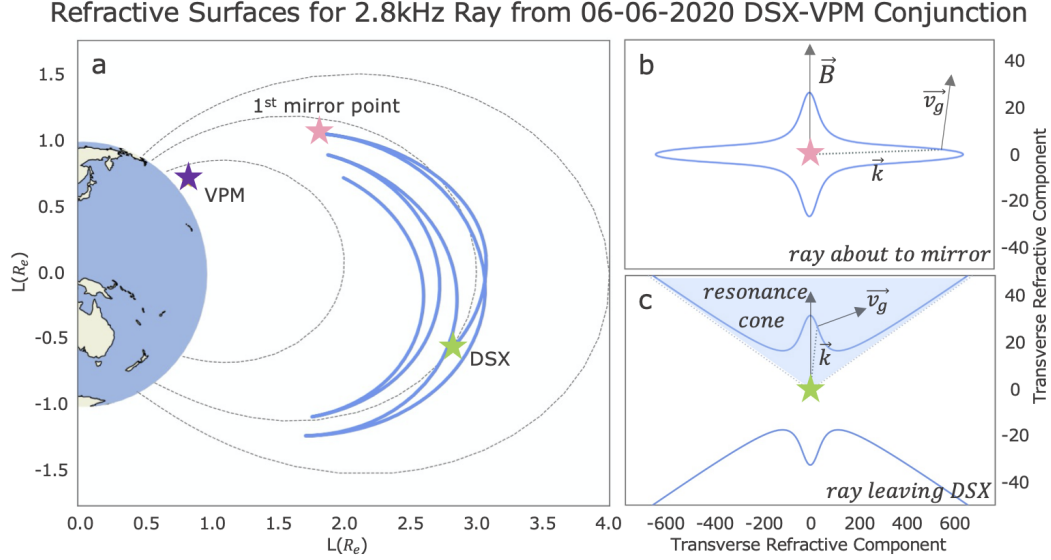


Figure 3. Ray propagation for the June 6, 2020 DSX-VPM conjunction with a 2.8 kHz transmission frequency. Panel a shows the propagation path in the meridional plane of a 2.8 kHz ray initialized at DSX. Panel c shows the refractive index surface at DSX and panel b shows the refractive index surface at its first mirror point. Panel c also shows the shaded resonance cone, within which all ray directions are initialized. Ray paths were computed in the Diffusive Equilibrium model.

290 ences the antenna radiation efficiency at arbitrary directions to the efficiency at the
 291 resonance cone, with a parabolic decay as the wave normal approaches field-aligned.

292 After the initial wave normal angle is defined and the magnitude of the initial in-
 293 dex of refraction, n_{DSX} , is found to compute η , the ray is then propagated towards LEO.
 294 Figure 3a shows the ray path. The ray's initial group velocity, and therefore the direc-
 295 tion of propagation, is normal to the refractive index surface at the intersection of the
 296 surface and the wave-vector. As the ray propagates, the refractive index surface changes
 297 with the changing medium, eventually closing in certain cases (shown in Figure 3b) and
 298 allowing the ray to mirror. In the case shown, the ray mirrors several times, settling at
 299 an L-shell between 2.5 and 3, but never reaching VPM's altitude of 500 km.

300 With rays initialized and weighted based on their directions, each ray is addition-
 301 ally assigned a fraction of the total dissipated power depending on transmission frequency.
 302 For example, in the conjunction on August 17, 10 Watts was dissipated by the DSX trans-
 303 mitter, and each ray is assigned a power of $\frac{10}{k}$ Watts, where k is the total number of rays
 304 simulated. The total power dissipated is given by P and the total number of rays reach-
 305 ing LEO is given as m in Equation 2. Therefore $m \cdot P$ gives the total power arriving at
 306 LEO. As the rays propagate to LEO, normalized Landau damping, indicated as χ , is ap-
 307 plied to each ray to scale the expected attenuation and/or growth. The area around VPM
 308 at LEO is divided into grid cells, each with area A , and we sum the total number of rays
 309 in each cell to calculate the final signal intensity at LEO in Watts/m². This intensity
 310 is converted to electric field amplitude in V/m through Equation 2:

$$E = \sqrt{\frac{2}{c\epsilon_0 A} \frac{P}{n_{res}^2} \sum_i^m \frac{n_{i,DSX}^2 \chi_{i,LEO}}{n_{i,LEO}}} \quad (2)$$

311 where the index of refraction at LEO, n_{LEO} , the speed of light, c , and permittivity of
 312 free space, ϵ_0 , are used to convert from intensity to electric field amplitude.

313 4 Results

314 Table 1 summarizes the results of simulating the 27 magnetic conjunctions between
 315 DSX and VPM. Of these conjunctions, eleven are in the low-frequency regime (2–4 kHz),
 316 seven in the mid-frequency regime (~ 8 kHz), and nine in the high-frequency regime (28 kHz).
 317 Dissipated power used for each simulation depends on the frequency transmitted, with
 318 approximately 3 Watts dissipated in the low-frequency regime, 10 Watts dissipated in
 319 the mid-frequency regime, and 30 Watts in the high-frequency regime. Note that it is
 320 unlikely that all of this power translated into propagating electromagnetic waves, so our
 321 results are by definition an upper bound on predicted electric fields. The third and fourth
 322 columns present the percentage of all rays simulated that mirrored before reaching VPM’s
 323 altitude. For high-frequency conjunctions, this percentage is always zero, as the trans-
 324 mitted frequency is well above the lower hybrid resonance frequency in the ionosphere,
 325 and therefore, the rays do not mirror. For mid-frequency conjunctions, the signals do
 326 encounter regions where the local lower hybrid resonance frequency is above the trans-
 327 mission frequency as they propagate towards the ionosphere, resulting in magnetospheric
 328 reflection (Kimura, 1966). Columns five and six of Table 1 present the maximum pre-
 329 dicted amplitude that VPM may have observed at LEO, with simulations run in both
 330 plasmasphere models. Entries with “Missed spot” indicate VPM’s trajectory did not pass
 331 through any regions of non-zero predicted amplitude during the burst. On May 28, 2020
 332 and June 1, 2020, DSX’s estimated position (near an L-shell value of 4) is very near to
 333 the modelled plasmopause, causing non-physical behavior of the simulated rays in the
 334 GCPM model. These two cases were subsequently omitted in the GCPM model, but re-
 335 sults are presented in the Diffusive Equilibrium model.

336 The seventh column in Table 1 indicates the VPM receiver’s estimated sensitiv-
 337 ity at the transmission frequency. This sensitivity depends on the present spacecraft noise
 338 and the theoretical Doppler shift at the transmission frequency. We determined sensi-
 339 tivity using the method described in Section 2. VPM frequently suffered from solar panel
 340 noise in the 0–5 kHz range, making lower frequency signals challenging to detect. How-
 341 ever, we expect more amplitude spreading for high-frequency conjunctions due to the
 342 comparatively larger Doppler shift. The net effect of the spacecraft noise and amplitude
 343 spreading is a consistent minimum detectable signal between $0.5 \mu\text{V}/\text{m}$ and $1 \mu\text{V}/\text{m}$ for
 344 all frequency regimes. In just two instances, the burst data was affected by abnormal
 345 spacecraft noise, which increased the minimum detectable signal. The final two columns
 346 of Table 1 show the minimum field line distance between the two satellites during each
 347 burst and the minimum transverse distance, or distance between VPM and DSX’s field
 348 line footprint at VPM’s altitude.

349 For all eleven of the low-frequency regime conjunctions (transmissions below 4 kHz),
 350 nearly 100% of the simulated rays mirrored before reaching VPM (see Figure 3) in both
 351 plasmasphere models, resulting in very low predicted electric field amplitudes at LEO.
 352 Because of this, example results from a low-frequency conjunction are not presented. In
 353 the mid-frequency regime, results are more variable. In some cases, such as May 8, 2020,
 354 results are similar to the low-frequency regime in which mirroring is the dominant be-
 355 havior for all simulated rays. However, for some mid-frequency conjunctions, mirroring
 356 strongly depends on the initial wave normal angle of the ray.

357 Highly oblique rays (wave normal angles near the resonance cone angle) are more
 358 likely to mirror before reaching LEO. This behavior is highlighted by the conjunction
 359 on May 19, 2020, shown in Figure 4. Figure 4 shows the result of propagating 100,000
 360 rays from DSX toward VPM in the Diffusive Equilibrium model. Figure 4a shows the
 361 wave normal distribution of the 46% of rays that mirrored before reaching LEO. Figure 4b

Table 1. Simulation Results of DSX-VPM Conjunctions

Date and Time (UT)	Freq.	% Mirror DE	% Mirror GCPM	Amp. DE	Amp. GCPM	Est. Sens.	Field line Dist. [km]	Transverse Dist. [km]
06 Apr 2020 22:04:45	8.2 kHz	79%	47%	1 $\mu\text{V}/\text{m}$	5 $\mu\text{V}/\text{m}$	1 $\mu\text{V}/\text{m}$	10065	38
26 Apr 2020 07:05:05	28 kHz	0%	0%	Missed spot	Missed spot	0.4 $\mu\text{V}/\text{m}$	24223	1
08 May 2020 21:49:20	8.2 kHz	100%	99%	0 $\mu\text{V}/\text{m}$	2 $\mu\text{V}/\text{m}$	5 $\mu\text{V}/\text{m}$	26942	594
10 May 2020 02:38:31	28 kHz	0%	0%	6 $\mu\text{V}/\text{m}$	20 $\mu\text{V}/\text{m}$	2 $\mu\text{V}/\text{m}$	13719	295
16 May 2020 12:04:15	28 kHz	0%	0%	Missed spot	Missed spot	0.5 $\mu\text{V}/\text{m}$	15649	172
19 May 2020 15:47:45	8.2 kHz	46%	32%	1 $\mu\text{V}/\text{m}$	3 $\mu\text{V}/\text{m}$	0.3 $\mu\text{V}/\text{m}$	6717	124
20 May 2020 18:27:45	28 kHz	0%	0%	11 $\mu\text{V}/\text{m}$	12 $\mu\text{V}/\text{m}$	0.5 $\mu\text{V}/\text{m}$	8518	315
25 May 2020 22:47:40	28 kHz	0%	0%	10 $\mu\text{V}/\text{m}$	15 $\mu\text{V}/\text{m}$	0.5 $\mu\text{V}/\text{m}$	14810	197
28 May 2020 02:19:30	28 kHz	0%	–	4 $\mu\text{V}/\text{m}$	–	0.5 $\mu\text{V}/\text{m}$	10828	196
29 May 2020 22:43:05	8.2 kHz	89%	29%	Missed spot	Missed spot	1 $\mu\text{V}/\text{m}$	11206	2292
01 Jun 2020 01:46:50	28 kHz	0%	–	3 $\mu\text{V}/\text{m}$	–	1 $\mu\text{V}/\text{m}$	11726	831
03 Jun 2020 13:46:25	3.0 kHz	95%	91%	0.2 $\mu\text{V}/\text{m}$	Missed spot	1 $\mu\text{V}/\text{m}$	10910	1810
06 Jun 2020 10:40:10	3.4 kHz	88%	64%	0.3 $\mu\text{V}/\text{m}$	1 $\mu\text{V}/\text{m}$	0.5 $\mu\text{V}/\text{m}$	9288	959
06 Jun 2020 19:56:10	2.8 kHz	100%	95%	0.2 $\mu\text{V}/\text{m}$	0.5 $\mu\text{V}/\text{m}$	0.5 $\mu\text{V}/\text{m}$	20362	1976
07 Jun 2020 17:49:15	3.4 kHz	97%	91%	0.2 $\mu\text{V}/\text{m}$	1 $\mu\text{V}/\text{m}$	0.5 $\mu\text{V}/\text{m}$	11824	587
16 Jun 2020 13:00:30	2.8 kHz	98%	89%	0.2 $\mu\text{V}/\text{m}$	0.3 $\mu\text{V}/\text{m}$	1 $\mu\text{V}/\text{m}$	13484	323
17 Jun 2020 15:37:20	3.2 kHz	95%	91%	0.2 $\mu\text{V}/\text{m}$	1 $\mu\text{V}/\text{m}$	0.5 $\mu\text{V}/\text{m}$	11307	208
18 Jun 2020 22:53:45	2.8 kHz	99%	83%	0.1 $\mu\text{V}/\text{m}$	0.5 $\mu\text{V}/\text{m}$	1 $\mu\text{V}/\text{m}$	15878	313
21 Jun 2020 19:44:35	3.4 kHz	98%	86%	0.2 $\mu\text{V}/\text{m}$	0.4 $\mu\text{V}/\text{m}$	0.5 $\mu\text{V}/\text{m}$	12608	266
04 Jul 2020 12:35:20	8.2 kHz	100%	60%	0 $\mu\text{V}/\text{m}$	2 $\mu\text{V}/\text{m}$	1 $\mu\text{V}/\text{m}$	27555	1092
23 Jul 2020 21:24:05	3.0 kHz	97%	97%	0.2 $\mu\text{V}/\text{m}$	Missed spot	0.5 $\mu\text{V}/\text{m}$	12608	2108
25 Jul 2020 00:04:50	8.2 kHz	96%	39%	0.5 $\mu\text{V}/\text{m}$	7 $\mu\text{V}/\text{m}$	1 $\mu\text{V}/\text{m}$	13138	168
27 Jul 2020 20:53:55	28 kHz	0%	0%	5 $\mu\text{V}/\text{m}$	20 $\mu\text{V}/\text{m}$	0.5 $\mu\text{V}/\text{m}$	13867	280
08 Aug 2020 15:09:05	3.6 kHz	62%	51%	0.3 $\mu\text{V}/\text{m}$	1 $\mu\text{V}/\text{m}$	1 $\mu\text{V}/\text{m}$	7403	477
08 Aug 2020 23:55:55	3.3 kHz	100%	91%	0 $\mu\text{V}/\text{m}$	0.5 $\mu\text{V}/\text{m}$	1 $\mu\text{V}/\text{m}$	17538	56
17 Aug 2020 21:20:35	8.8 kHz	43%	20%	1 $\mu\text{V}/\text{m}$	2 $\mu\text{V}/\text{m}$	1 $\mu\text{V}/\text{m}$	7184	324
20 Aug 2020 18:34:50	28 kHz	0%	0%	5 $\mu\text{V}/\text{m}$	10 $\mu\text{V}/\text{m}$	0.5 $\mu\text{V}/\text{m}$	7119	724

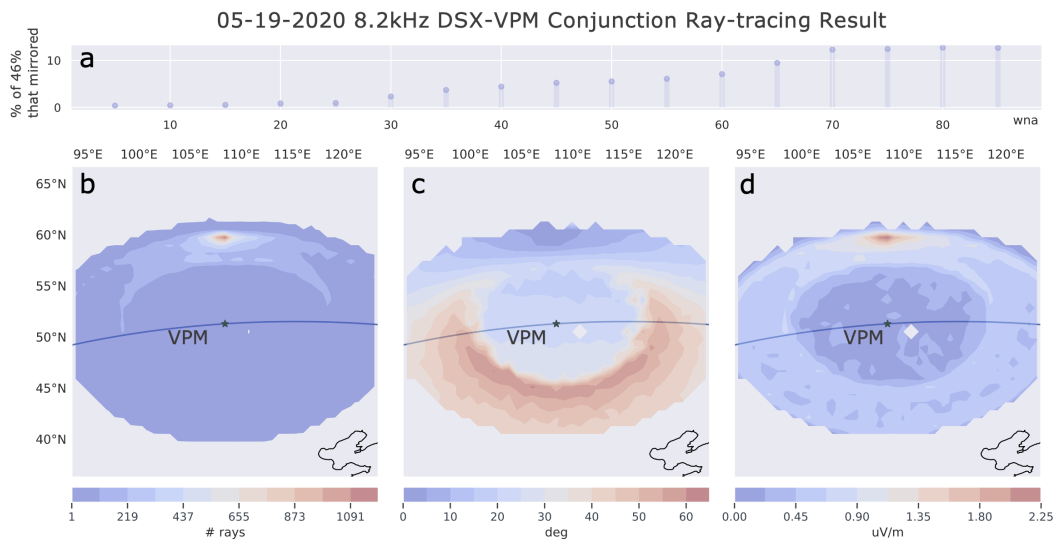


Figure 4. Ray-tracing result in the Diffusive Equilibrium model from the May 19, 2020 DSX-VPM conjunction with an 8.2 kHz transmission frequency. Panel a is a histogram showing the wave normal angle distribution of the rays that mirrored before reaching LEO. Panel b shows the number of rays arriving at LEO and the panel c is a contour plot of the average initial wave normal angle of those rays. Panel d shows electric field amplitude calculated from Equation 2. The grey regions of these plots are where the ray count is zero.

362 indicates the ray density at LEO, while the Figure 4c shows the average initial wave normal
 363 angle of the rays reaching LEO in each latitude / longitude bin. Figure 4d shows
 364 predicted electric field amplitude, after taking into account the distribution of initial wave
 365 normal angles. VPM is shown as the dark star moving along its ground track shown in
 366 blue.

367 Figure 5 also shows the ray paths for this exact conjunction in the meridional plane,
 368 with line color indicating initial wave normal angle. Comparing these two figures, we can
 369 see how most field-aligned rays propagate toward LEO and end up at slightly higher lat-
 370 itudes than oblique rays, which mostly follow the magnetic field line traced from DSX.
 371 While some of these rays reach LEO, considerably more highly oblique rays mirror, and
 372 continue to mirror multiple times and settle in the magnetosphere. When comparing Fig-
 373 ure 4c and Figure 4d, we see how most rays that reach LEO are nearly field-aligned. There-
 374 fore, the resulting electric field amplitude is highest at the region of high ray density/
 375 low initial wave normal angle rather than where the fewer highly oblique rays reach LEO.

376 Predicted amplitudes for the May 19, 2020 conjunction are near or below the es-
 377 timated VPM sensitivity and are relatively consistent between plasmasphere models. In
 378 other mid-frequency conjunctions with wave normal dependence on mirroring, the two
 379 plasmasphere models produce significantly different results for the same conjunction, dis-
 380 cussed further in Section 5.

381 We also present the results of ray-tracing for a high-frequency conjunction on July
 382 27, 2020. In this conjunction, the ray frequency is too high for the refractive surface to
 383 close, and the rays do not mirror. Therefore, the location of the highest ray intensity rel-
 384 ative to VPM is the most critical consideration. Results in the Diffusive Equilibrium model
 385 are presented in Figure 6, with a maximum electric field amplitude of $8 \mu\text{V/m}$ predicted.
 386 VPM's trajectory, however, only passes through an area where the amplitude peaks at

05-19-2020 8.2kHz DSX-VPM Conjunction Meridional Plane

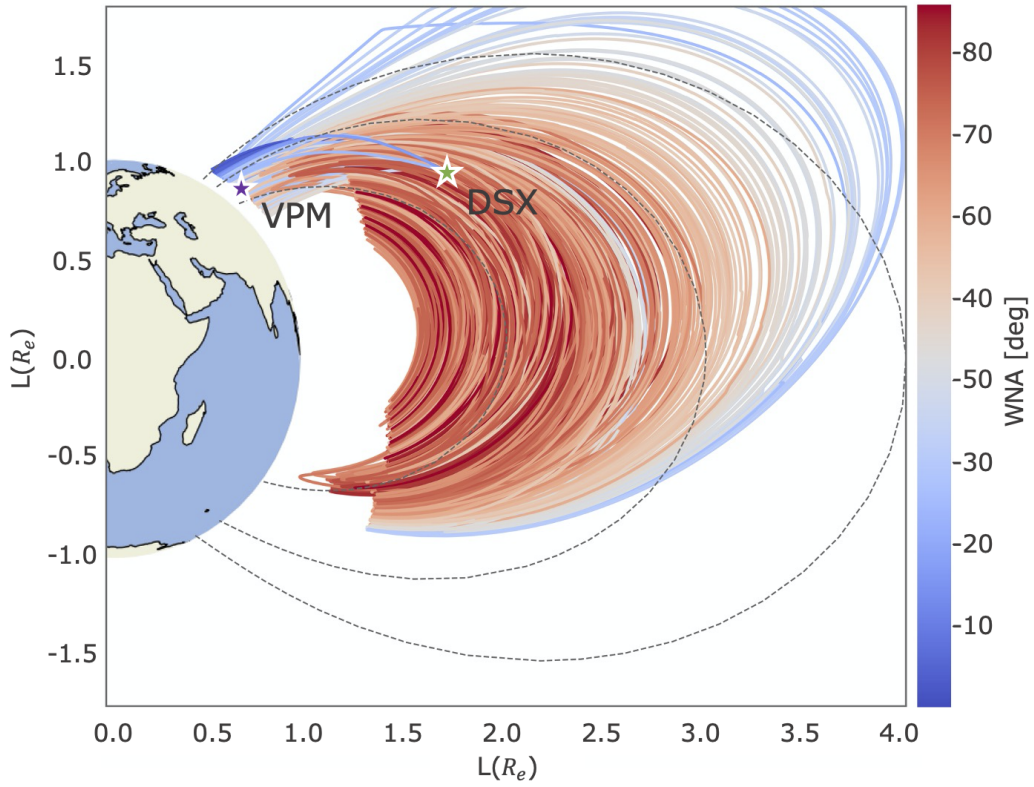


Figure 5. Meridional plane view of the May 19, 2020 DSX-VPM conjunction with an 8.2 kHz transmission frequency. Ray paths are computed in the Diffusive Equilibrium model and are shown from DSX to VPM, with the color of the path indicating the initial wave normal angle.

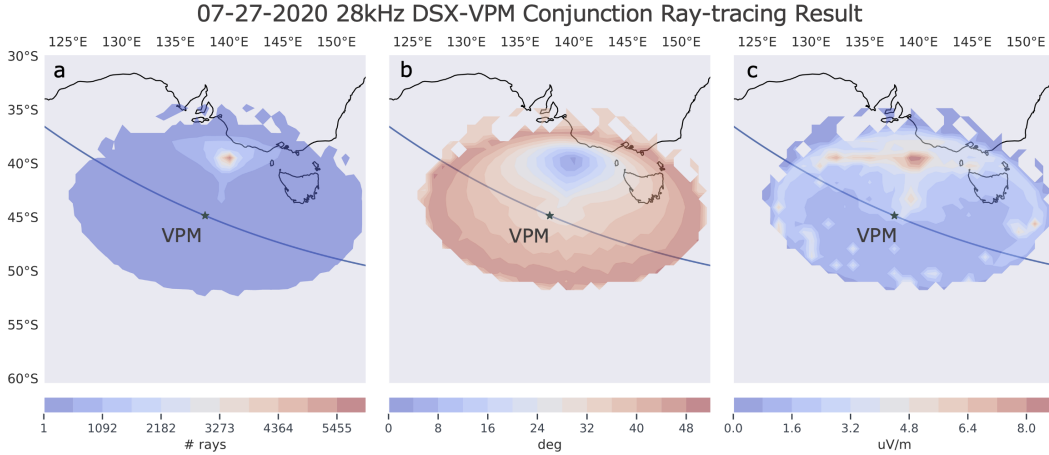


Figure 6. Ray-tracing result in the Diffusive Equilibrium model from the July 27, 2020 DSX-VPM conjunction with a 28 kHz transmission frequency. Panel a shows number of rays arriving at LEO and panel b is a contour plot of the average initial wave normal angle of those rays. Panel c shows electric field amplitude calculated from Equation 2. The grey regions of these plots are where the ray count is zero. A histogram showing wave normal angle distribution of rays that mirrored is not included because rays do not mirror at this frequency.

387 5 $\mu\text{V}/\text{m}$. A similar trend is seen where field-aligned rays are found in the highest intensi-
 388 sity, with higher wave normal rays spread into the region around this area. Most other
 389 high-frequency conjunctions resulted in similar amplitudes and were consistent between
 390 plasmasphere models.

391 5 Discussion and Conclusions

392 Results indicate that low-frequency transmissions were unlikely to be observed by
 393 VPM, while some mid-frequency and most high-frequency transmission conjunctions are
 394 predicted to have amplitudes above a few $\mu\text{V}/\text{m}$ given our assumptions about the trans-
 395 mitter power. The DSX dissipated powers used here impose an absolute upper bound
 396 on amplitudes. The minimum detectable signal is between 0.5 $\mu\text{V}/\text{m}$ and 1 $\mu\text{V}/\text{m}$. While
 397 these results seem to suggest that VPM should have observed the DSX signal, there are
 398 two possible explanations for this discrepancy. First, the antenna radiation efficiency at
 399 DSX is a source of uncertainty in this method. We expect that high wave normal angles
 400 are the most efficiently excited by the DSX transmitter. As such, we have weighted
 401 the antenna radiation efficiency, η , based on wave normal angle as described in Section 3.
 402 However, based on discussions and modelling of the DSX antenna, it is likely that our
 403 radiation efficiency overestimates the power in low wave normal (field-aligned) rays, re-
 404 sulting in a higher electric field amplitude predicted at LEO. Ongoing work is attempt-
 405 ing to estimate a more accurate radiation pattern for the DSX transmitting antenna.

406 In fact, the choice of radiation efficiency is very significant in the maximum predicted
 407 electric field amplitude. Figure 7 compares predicted electric field amplitude at
 408 LEO for an 8.8 kHz transmission from DSX with three different antenna efficiencies. Fig-
 409 ure 7a shows an isotropic model, in which all wave normal angles are excited equally. The
 410 predicted amplitude is well above the minimum detectable signal. Figure 7b uses the an-
 411 tenna radiation efficiency η discussed in Section 3, proportional to the square of the in-
 412 dex of refraction. In this case the electric field amplitude is an order of magnitude lower
 413 compared to the isotropic radiator. Finally, with a more severe dependence on k-vector

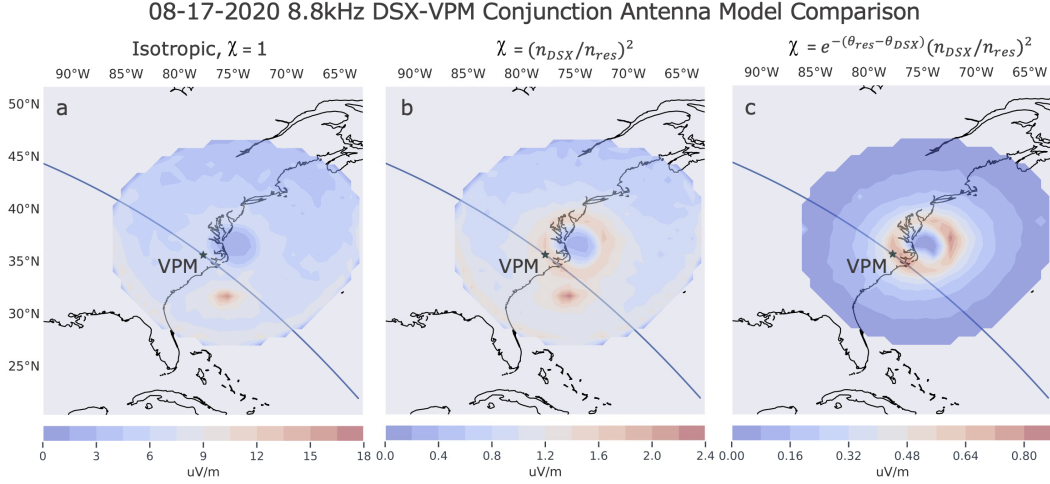


Figure 7. Electric field amplitude at LEO for the August 17, 2020 DSX-VPM conjunction with an 8.8 kHz transmission frequency comparing three antenna radiation efficiencies. Panel a shows an isotropic antenna model while panel b shows the antenna efficiency given in Equation 1. Panel c shows an antenna efficiency with a more severe dependence on k-vector direction. The grey regions of these plots are where the ray count is zero. Ray paths are computed in the GCPM model.

direction shown in Figure 7c, found by including an exponential decay expanded around the resonance cone angle, the predicted amplitude at LEO drops another order of magnitude. This factor represents an artificial adjustment to the physics-based radiation pattern given in Equation 1 and attempts to weight the radiation pattern even more heavily toward the resonance cone. While this model is not physics-based, this comparison shows how essential the initial radiation pattern is to predicting the final electric field amplitude.

The second explanation for the discrepancy between observations and simulated amplitudes is the plasmasphere model. Results from Figure 6 show a “spot” of highest intensity. The location and amplitude of this spot can vary drastically between plasmasphere models. In the GCPM model for the same simulation presented in Figure 6, the spot moves south nearly 500 km, closer to VPM’s trajectory, and the amplitude doubles. Given that models are estimates of the physical plasmasphere that may have existed during each conjunction, the two results represent simulation uncertainty. This uncertainty is further highlighted by Figure 8, which shows the predicted electric field amplitude for the conjunction occurring on July 25, 2020 with an 8.2 kHz transmission frequency. In the Diffusive Equilibrium model, 96% of the rays mirror before reaching LEO, while only 39% mirror in GCPM. This results in a maximum amplitude below 1 $\mu\text{V}/\text{m}$ for Diffusive Equilibrium, but up to 7 $\mu\text{V}/\text{m}$ for GCPM. We believe this is attributed to a slightly larger density gradient at LEO in the Diffusive Equilibrium model that results in a higher local lower hybrid resonance frequency. When this frequency exceeds that of the signals, the rays mirror.

The antenna efficiency or radiation pattern and the plasmasphere model are crucial parameters for experiments with inner magnetosphere VLF transmissions to LEO. Highly oblique rays are likely most efficiently excited by the DSX transmitter, which results in significant magnetospheric reflection (mirroring) and low amplitudes observed at LEO. For the attempted low-frequency conjunctions, this seems to be the most significant reason for not observing DSX, as the two plasmasphere models produced very

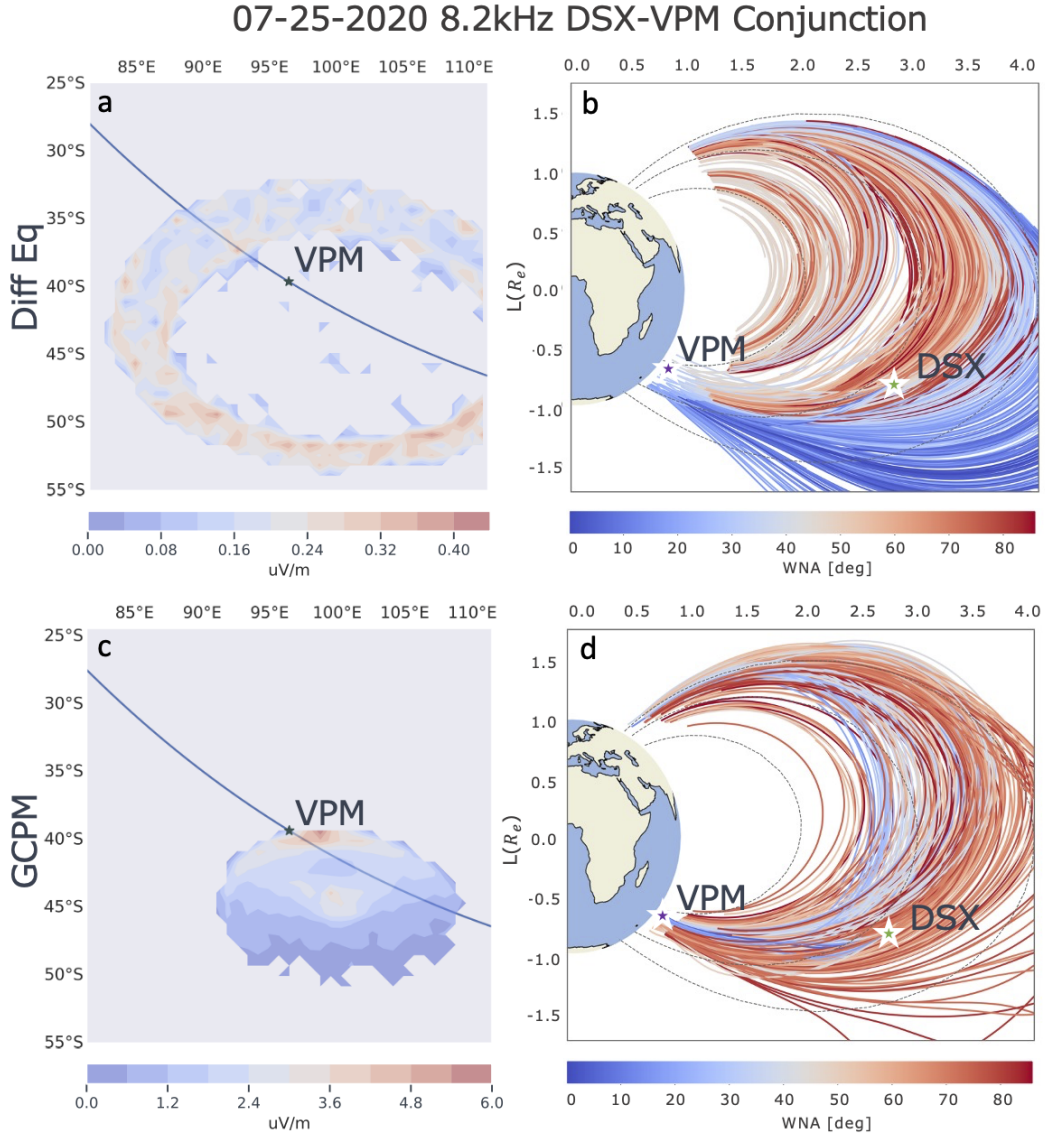


Figure 8. Electric field amplitude at LEO (panels a and c) and meridional plane view with initial wave normal angle shown on the color scale (panels b and d) for the July 25, 2020 DSX-VPM conjunction with an 8.2 kHz transmission frequency. Panels a and b present results from simulations in the Diffusive Equilibrium model while panels c and d present results from simulations in the GCPM model. The grey regions of panels a and c are where the ray count is zero.

similar results. In the mid-frequency regime, both the antenna model and the plasma-sphere model result in wide variation. The antenna model used is a critical driver in the final electric field amplitude, and we suspect Figure 7c is closest to the actual DSX antenna radiation pattern (also the smallest electric field amplitude). Ongoing work with the DSX data set should help to justify this. In addition, the present plasma density gradients can significantly impact the number of rays that mirror, resulting in a large range of possible amplitudes with high spatial uncertainty for these conjunctions. This uncertainty of the ray “spot” is the most likely reason for the lack of observation of the high-frequency conjunctions as well. While the actual DSX antenna pattern may drop the expected amplitudes, they may still be in the observable range (over $0.5 \mu\text{V/m}$), and therefore we conclude that in these cases VPM simply missed the ray spot.

6 Open Research

The VPM data used for analysis are available as a Zenodo repository via <https://doi.org/10.5281/zenodo.5522908>. The Stanford ray tracer used for ray tracing simulations is preserved at Zenodo via <https://zenodo.org/badge/latestdoi/217197448> and openly developed at https://github.com/rareid2/Stanford_Raytracer.

Acknowledgments

This work was supported under contract FA9453-19-C-0400 to Atmospheric and Environmental Research (AER), Incorporated and subcontract P2247-04 to the University of Colorado Boulder. Contract FA9453-12-C-0217 to Stanford University supported the design and build of the VPM payload, while the VPM spacecraft was built and operated by Air Force Research Laboratory. The entire DSX spacecraft was designed, built, and operated by the Air Force Research Laboratory.

References

- Alken, P., Thébault, E., Beggan, C. D., Amit, H., Aubert, J., Baerenzung, J., . . . others (2021). International geomagnetic reference field: the thirteenth generation. *Earth, Planets and Space*, *73*(1), 1–25.
- Angerami, J., & Thomas, J. (1964). Studies of planetary atmospheres: 1. the distribution of electrons and ions in the Earth’s exosphere. *Journal of Geophysical Research*, *69*(21), 4537–4560.
- Bell, T. F., Inan, U. S., Bortnik, J., & Scudder, J. (2002). The landau damping of magnetospherically reflected whistlers within the plasmasphere. *Geophysical Research Letters*, *29*(15), 23–1.
- Bilitza, D. (2001). International reference ionosphere 2000. *Radio Science*, *36*(2), 261–275.
- Bortnik, J. (2004). *Precipitation of radiation belt electrons by lightning-generated magnetospherically reflecting whistler waves*. Stanford University.
- Bortnik, J., Thorne, R., Meredith, N., & Santolik, O. (2007). Ray tracing of penetrating chorus and its implications for the radiation belts. *Geophysical Research Letters*, *34*(15).
- Brinca, A. (1972). On the stability of obliquely propagating whistlers. *Journal of Geophysical Research*, *77*(19), 3495–3507.
- Carpenter, D., & Anderson, R. (1992). An ISEE/whistler model of equatorial electron density in the magnetosphere. *Journal of Geophysical Research: Space Physics*, *97*(A2), 1097–1108.
- Cohen, M. B., & Inan, U. (2012). Terrestrial VLF transmitter injection into the magnetosphere. *Journal of Geophysical Research: Space Physics*, *117*(A8).
- Colpitts, C., Miyoshi, Y., Kasahara, Y., Delzanno, G. L., Wygant, J. R., Cattell, C. A., . . . others (2020). First direct observations of propagation of discrete

- 491 chorus elements from the equatorial source to higher latitudes, using the Van
 492 Allen probes and Arase satellites. *Journal of Geophysical Research: Space*
 493 *Physics*, 125(10), e2020JA028315.
- 494 Gallagher, D. L., Craven, P. D., & Comfort, R. H. (2000). Global core plasma
 495 model. *Journal of Geophysical Research: Space Physics*, 105(A8), 18819–
 496 18833.
- 497 Horne, R., Glauert, S., Meredith, N., Boscher, D., Maget, V., Heynderickx, D., &
 498 Pitchford, D. (2013). Space weather impacts on satellites and forecasting the
 499 Earth’s electron radiation belts with SPACECAST. *Space Weather*, 11(4),
 500 169–186.
- 501 Inan, U., & Bell, T. (1977). The plasmopause as a VLF wave guide. *Journal of Geo-*
 502 *physical Research*, 82(19), 2819–2827.
- 503 Inan, U., Bell, T., Bortnik, J., & Albert, J. (2003). Controlled precipitation of radia-
 504 tion belt electrons. *Journal of Geophysical Research: Space Physics*, 108(A5).
- 505 Kimura, I. (1966). Effects of ions on whistler-mode ray tracing. *Radio Science*, 1(3),
 506 269–283.
- 507 Kulkarni, P., Inan, U., Bell, T., & Bortnik, J. (2007). Dependence of whistler-mode
 508 wave induced electron precipitation on k-vector direction. In *AGU Fall Meet-*
 509 *ing Abstracts* (Vol. 2007, pp. SM33B–1340).
- 510 Kulkarni, P., Inan, U., Bell, T., & Bortnik, J. (2008). Precipitation signatures
 511 of ground-based VLF transmitters. *Journal of Geophysical Research: Space*
 512 *Physics*, 113(A7).
- 513 Ma, Q., Mourenas, D., Li, W., Artemyev, A., & Thorne, R. M. (2017). VLF waves
 514 from ground-based transmitters observed by the Van Allen Probes: Statistical
 515 model and effects on plasmaspheric electrons. *Geophysical Research Letters*,
 516 44(13), 6483–6491.
- 517 Marshall, R. A., Sousa, A., Reid, R., Wilson, G., Starks, M., Ramos, D., ... others
 518 (2021). The micro-broadband receiver (μ bbr) on the very-low-frequency propa-
 519 gation mapper cubesat. *Earth and Space Science*, 8(11), e2021EA001951.
- 520 Némec, F., Santolík, O., & Parrot, M. (2021). Doppler shifted alpha transmitter
 521 signals in the conjugate hemisphere: DEMETER spacecraft observations and
 522 raytracing modeling. *Journal of Geophysical Research: Space Physics*, 126(4),
 523 e2020JA029017.
- 524 Rodger, C. J., Carson, B. R., Cummer, S. A., Gamble, R. J., Clilverd, M. A.,
 525 Green, J. C., ... Berthelier, J.-J. (2010). Contrasting the efficiency of ra-
 526 diation belt losses caused by ducted and nonducted whistler-mode waves from
 527 ground-based transmitters. *Journal of Geophysical Research: Space Physics*,
 528 115(A12).
- 529 Sauvaud, J.-A., Maggiolo, R., Jacquey, C., Parrot, M., Berthelier, J.-J., Gamble, R.,
 530 & Rodger, C. J. (2008). Radiation belt electron precipitation due to VLF
 531 transmitters: Satellite observations. *Geophysical Research Letters*, 35(9).
- 532 Scherbarth, M., Smith, D., Adler, A., Stuart, J., & Ginet, G. (2009). AFRL’s
 533 Demonstration and Science Experiments (DSX) mission. In *Solar physics and*
 534 *space weather instrumentation iii* (Vol. 7438, p. 74380B).
- 535 Shklyar, D., Parrot, M., Chum, J., Santolik, O., & Titova, E. (2010). On the origin
 536 of lower-and upper-frequency cutoffs on wedge-like spectrograms observed by
 537 DEMETER in the midlatitude ionosphere. *Journal of Geophysical Research:*
 538 *Space Physics*, 115(A5).
- 539 Sousa, A. P. (2018). *Global and seasonal effects of lightning-induced electron precipi-*
 540 *tation*. Stanford University.
- 541 Spanjers, G., Winter, J., Cohen, D., Adler, A., Guarnieri, J., Tolliver, M., ... Sum-
 542 mers, J. (2006). The AFRL Demonstration and Science Experiments (DSX)
 543 for DoD space capability in the MEO. In *2006 IEEE Aerospace Conference*
 544 (pp. 10–pp).
- 545 Starks, M., Albert, J., Ling, A., O’Malley, S., & Quinn, R. (2020). VLF transmitters

- 546 and lightning-generated whistlers: 1. modeling waves from source to space.
547 *Journal of Geophysical Research: Space Physics*, 125(3), e2019JA027029.
- 548 Starks, M., Bell, T. F., Quinn, R., Inan, U. S., Piddychiy, D., & Parrot, M. (2009).
549 Modeling of Doppler-shifted terrestrial VLF transmitter signals observed by
550 DEMETER. *Geophysical Research Letters*, 36(12).
- 551 Verronen, P. T., Andersson, M. E., Rodger, C. J., Clilverd, M. A., Wang, S., & Tu-
552 runen, E. (2013). Comparison of modeled and observed effects of radiation
553 belt electron precipitation on mesospheric hydroxyl and ozone. *Journal of*
554 *Geophysical Research: Atmospheres*, 118(19), 11–419.
- 555 Zhang, Z., Chen, L., Li, X., Xia, Z., Heelis, R. A., & Horne, R. B. (2018). Observed
556 propagation route of VLF transmitter signals in the magnetosphere. *Journal of*
557 *Geophysical Research: Space Physics*, 123(7), 5528–5537.